Article

Direct radiative effects of airborne microplastics

https://doi.org/10.1038/s41586-021-03864-x

Received: 24 January 2021

Accepted: 29 July 2021

Published online: 20 October 2021

Check for updates

Laura E. Revell[1]✉, Peter Kuma[1,3], Eric C. Le Ru[2], Walter R. C. Somerville[2] & Sally Gaw[1]

Microplastics are now recognized as widespread contaminants in the atmosphere, where, due to their small size and low density, they can be transported with winds around the Earth[1–25]. Atmospheric aerosols, such as mineral dust and other types of airborne particulate matter, influence Earth's climate by absorbing and scattering radiation (direct radiative effects) and their impacts are commonly quantified with the effective radiative forcing (ERF) metric[26]. However, the radiative effects of airborne microplastics and associated implications for global climate are unknown. Here we present calculations of the optical properties and direct radiative effects of airborne microplastics (excluding aerosol–cloud interactions). The ERF of airborne microplastics is computed to be 0.044 ± 0.399 milliwatts per square metre in the present-day atmosphere assuming a uniform surface concentration of 1 microplastic particle per cubic metre and a vertical distribution up to 10 kilometres altitude. However, there are large uncertainties in the geographical and vertical distribution of microplastics. Assuming that they are confined to the boundary layer, shortwave effects dominate and the microplastic ERF is approximately −0.746 ± 0.553 milliwatts per square metre. Compared with the total ERF due to aerosol–radiation interactions[27] (−0.71 to −0.14 watts per square metre), the microplastic ERF is small. However, plastic production has increased rapidly over the past 70 years[28]; without serious attempts to overhaul plastic production and waste-management practices, the abundance and ERF of airborne microplastics will continue to increase.

Since large-scale production of plastics began in the 1950s, around 5 Gt of plastic waste has accumulated in landfills or the environment[28]. Plastics become brittle as they age and may break down to produce microplastics and nanoplastics, typically defined as particles 1–5,000 μm and <1 μm in size, respectively. Microplastics are ubiquitous pollutants in aquatic and terrestrial environments[29,30]. Primary sources of microplastics include pre-production pellets or nurdles used in the manufacture of plastic items and microbeads in personal care products, abrasive cleaning products, paint and blasting abrasives. Secondary sources include synthetic fabric fibres, dust from synthetic rubber tyres, paint particles and the degradation of larger plastics that become brittle through exposure to UV radiation[25,31]. When inhaled in ambient air, micro- and nanoplastics may pose a threat to human health[32].

Measurements of airborne microplastics

In recent years, airborne microplastics have been detected around the world (for example, refs. [1–23]). Common polymers detected in air include polyester, polyethylene, polypropylene, acrylic and resins (Extended Data Fig. 1). Airborne microplastics are typically collected by pumped air samplers, which yield a number concentration, or by collecting atmospheric fallout, yielding a deposition flux. Reported number concentrations of airborne microplastics to date are summarized in Fig. 1. Concentrations range between 0.01 microplastic particle (MP) m^{-3} (West Pacific Ocean[15]) to 5,650 MP m^{-3} (Beijing, China[13]). In contrast, total aerosol number concentrations over Europe and East Asia are typically on the order of 1×10^9–1×10^{10} m^{-3}, so microplastics are a relatively small component of total aerosol abundance[33]. It should be noted that no standardized procedure for sampling and analysing airborne microplastics exists, and comparisons of different studies must be made with caution. Nonetheless, measured concentrations of airborne microplastics vary by orders of magnitude depending on the sampling site, meteorological conditions and analytical methods used.

The highest reported concentrations of microplastics (thousands of MP m^{-3}) were measured in London, United Kingdom[12], and Beijing, China[13]. These studies used Raman spectral imaging and scanning electron microscopy-energy dispersive X-ray (SEM-EDX) spectroscopy, respectively, to detect airborne microplastics. In both studies, approximately half of the microplastics detected were between 5 and 10 μm in size. This size range is below the 11 μm detection limit of micro-Fourier transform infrared (μFTIR) spectroscopy, which was used in the majority of the other studies represented in Fig. 1. However, the high concentrations measured are also probably due to the locations of the sampling sites, which were urban sites in megacities. Reported concentrations of airborne microplastics are typically lower in remote environments compared with urban environments—for example,

[1]School of Physical and Chemical Sciences, University of Canterbury, Christchurch, New Zealand. [2]The MacDiarmid Institute for Advanced Materials and Nanotechnology, School of Chemical and Physical Sciences, Victoria University of Wellington, Wellington, New Zealand. [3]Present address: Department of Meteorology, Stockholm University, Stockholm, Sweden. ✉e-mail: laura.revell@canterbury.ac.nz

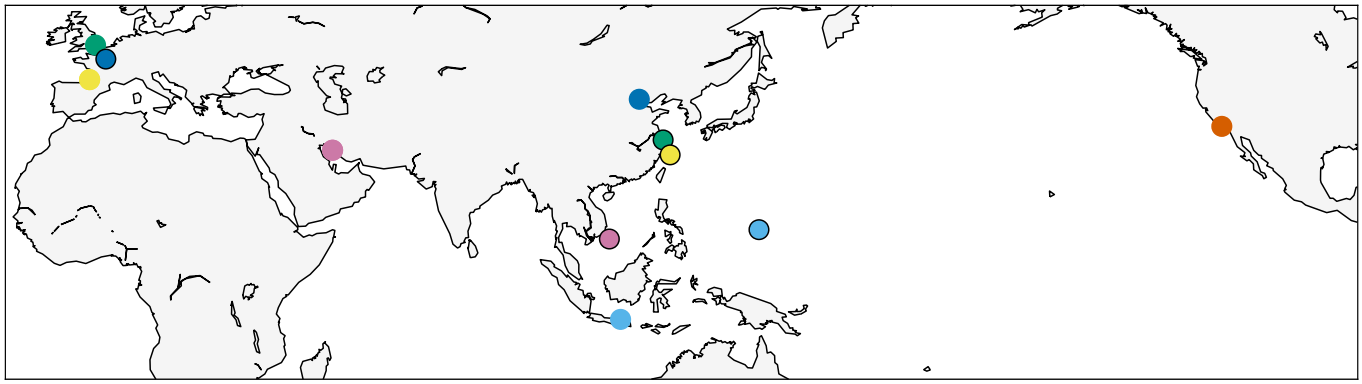

Location	Concentration (MP m^{-3})	Analytical method
Beijing, China[13]	5,650	SEM-EDX
London, United Kingdom[12]	2,502	Raman spectral imaging
Surabaya, Indonesia[20]	109	FTIR
Bushehr Port, Iran (dusty days)[1]	10.3	μRaman
French Atlantic Coast (offshore wind)[3]	9.6	μRaman
Southern California[9]	6.2	μRaman and μFTIR
French Atlantic Coast (onshore wind)[3]	2.9	μRaman
Bushehr Port, Iran (normal days)[1]	2.1	μRaman
Shanghai, China[14]	1.42	μFTIR
Paris, France[8]	0.9	μFTIR
East China Sea[15]	0.13	μFTIR
South China Sea and West Pacific Ocean[17]	0.11	μFTIR
West Pacific Ocean[15]	0.01	μFTIR

Fig. 1 | Concentrations of airborne microplastics reported by previous studies. All studies relied on pumped air (active) sampling rather than deposition collection (passive sampling), and all studies confirmed polymer composition spectroscopically via either FTIR, micro-Raman (μRaman) or SEM-EDX spectroscopy. The mean and median concentrations are 638 and 2.9 MP m^{-3}, respectively. Map data sourced from https://www.soest.hawaii.edu/pwessel/gshhg/ (ref. [47]) and plotted using Python[48].

measurements[15] over the remote ocean have been reported on the order of 0.01 MP m^{-3}. Similarly, the concentration of microplastics measured on the French Atlantic coast in onshore winds was reported to be on average one-third of that measured in offshore winds[3].

Typically ranging between 15 and 250 μm in size (Extended Data Figs. 2, 3), airborne microplastics are one to two orders of magnitude larger than other types of atmospheric aerosol, which usually have diameters smaller than 2.5 μm. However, their low density (between 0.86 g cm^{-3} for polyethylene to 1.38 g cm^{-3} for polyethylene terephthalate and polyvinyl chloride, Extended Data Fig. 1) means that they are easily entrained[34] and transported over large distances[24]. Given their hydrophobicity, they may be less likely to be deposited via cloud formation and precipitation compared with airborne particles of a similar size. Similar deposition fluxes of airborne microplastics were recorded in central Paris[7] and a remote mountain catchment in the French Pyrenees, far from any major population centre[2]. Modelling shows that microplastics generated from road traffic (tire wear particles and brake wear particles) have high transport efficiencies to remote regions[25]. Furthermore, it has been suggested that such particles may contribute to warming of the cryosphere owing to their light-absorbing properties[25].

Atmospheric aerosols scatter and absorb solar and terrestrial radiation[26], leading to atmospheric warming or cooling depending on particle size, shape, composition and atmospheric and surface conditions. Overall, direct aerosol–radiation interactions have a negative effective radiative forcing (ERF; that is, a cooling influence on surface climate); however, black carbon aerosol has a positive ERF and causes warming because it is highly absorbing of solar radiation[26]. Here we present an approximation of the direct global radiative effects of airborne microplastics. We calculated the optical properties of non-pigmented fragments and fibres, the two most common microplastic shapes (Extended Data Fig. 4), and included the optical properties in a general circulation model (GCM) to calculate the ERF of airborne microplastics (see Methods).

Microplastic optical properties and ERF

The scattering cross-sections of non-pigmented microplastic fragments and fibres (Fig. 2) indicate that microplastics are efficient at scattering ultraviolet (UV) and visible radiation, which by itself would have a cooling influence on surface climate. However, the absorption cross-sections indicate that microplastics absorb infrared radiation, including in the 'atmospheric window' between 8 and 12 μm where few other species absorb in Earth's atmosphere. Microplastics may therefore contribute to the greenhouse effect. Overall, microplastics predominantly scatter in the UV and visible regions as indicated by the single scattering albedo (Fig. 2), whereas in the infrared they absorb radiation almost as much as they scatter it.

GCM simulations performed with approximately the median microplastic concentration from Fig. 1 (1 MP m^{-3} uniformly distributed at the surface globally, with vertical scaling applied; see Methods) did not yield a clear signal-to-noise ratio in ERF in a 20-yr simulation. Instead, simulations were performed assuming 100 MP m^{-3} at the surface, which is on the same order of magnitude as the mean concentration from Fig. 1 of 638 MP m^{-3}. The resulting ERFs are shown in Fig. 3a, and compared with the radiative forcing (RF) of common aerosol components as reported in the Intergovernmental Panel on Climate Change's Fifth Assessment Report (IPCC AR5)[26].

Non-pigmented microplastic fragments and fibres simulated with a near-surface concentration of 100 MP m^{-3} exert longwave ERFs of +0.164 ± 0.086 and +0.229 ± 0.110 W m^{-2}, respectively (Fig. 3b). Fragments and fibres exert shortwave ERFs of −0.183 ± 0.088 and −0.268 ± 0.066 W m^{-2}, respectively. Both findings are consistent with the absorption and scattering cross-sections presented in Fig. 2. Since microplastics are large compared with other anthropogenic or natural aerosol particles, their effect on longwave radiation relative to their effect on shortwave radiation is expected to be larger than for other types of aerosol. Therefore, the longwave and shortwave effects almost

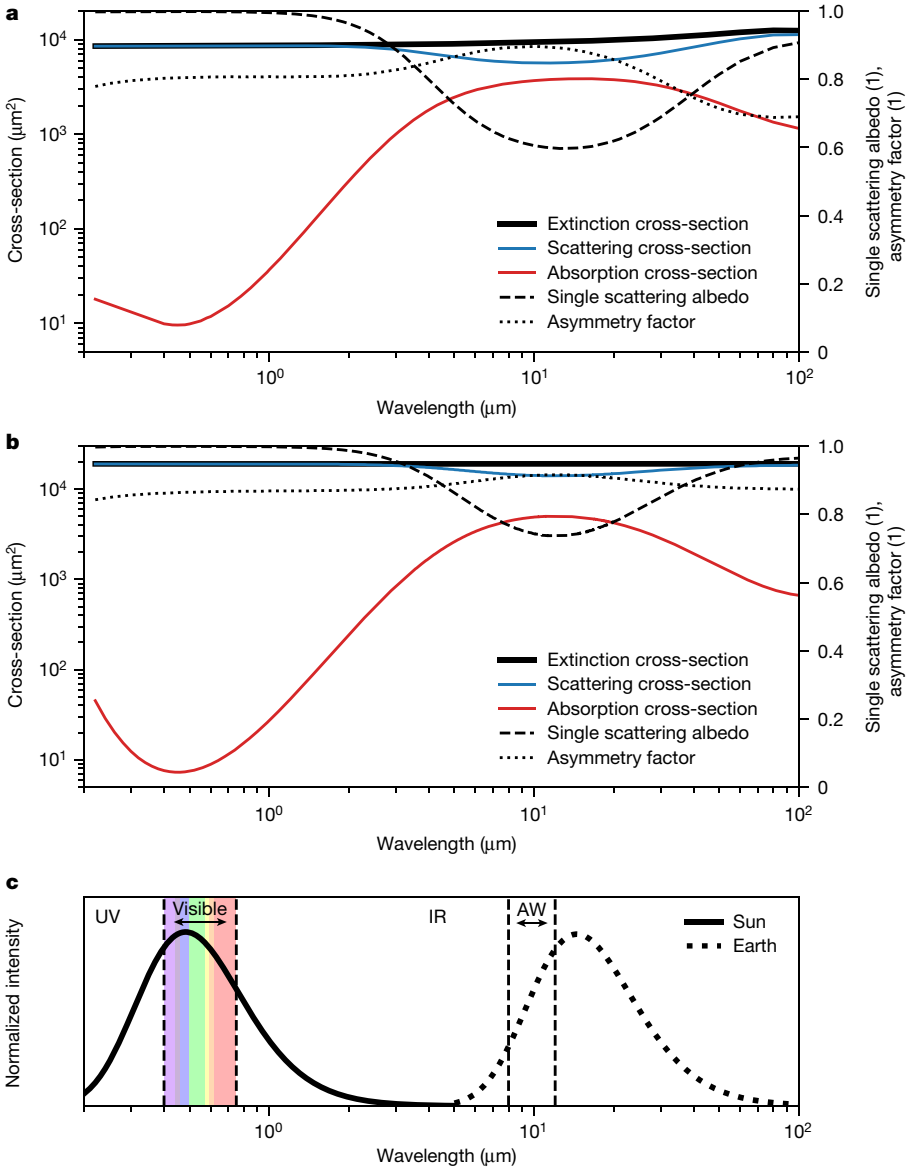

Fig. 2 | Optical properties of microplastic fragments and fibres. a, Fragment cross-sections (left *y* axis) and single scattering albedo and asymmetry factor (right *y* axis; (1) indicates dimensionless quantities) calculated by Mie theory assuming a theoretical gamma size distribution (Extended Data Fig. 2) and an idealized refractive index (Extended Data Fig. 5). **b**, As for **a**, but showing optical properties for fibres calculated assuming a theoretical gamma size distribution (Extended Data Fig. 3). **c**, Normalized intensity of blackbody radiation emitted by the Sun and Earth. AW denotes the infrared atmospheric window, the region between 8 and 12 μm where relatively little absorption of terrestrial radiation by greenhouse gases occurs aside from the ozone absorption band at 9.6 μm.

cancel when microplastics are assumed to be present up to 10 km altitude. Overall, fibres have a larger influence on shortwave and longwave ERF than fragments because fibres tend to be larger (Extended Data Figs. 2, 3). The net ERF in a combined simulation assuming 50 fragments per m^3 and 50 fibres per m^3 is 0.004 ± 0.040 W m^{-2} (that is, between −0.036 and +0.044 W m^{-2}). This result is similar in magnitude to the RF of secondary organic aerosol (−0.03 W m^{-2} in IPCC AR5[26]; however we note that secondary organic aerosol is the smallest forcing term of all aerosols considered by the IPCC, and that its ERF has more recently been estimated[35] to span a wide range from −0.01 to −0.78 W m^{-2}).

The uncertainty in the sign of the microplastic ERF arises from the shortwave and longwave ERFs having a similar magnitude for non-pigmented microplastics. Although 100 MP m^{-3} is a large surface concentration to prescribe globally, it is far below the highest concentration of airborne microplastics reported (Fig. 1). We selected 100 MP m^{-3} to separate signal from noise, as discussed earlier. Assuming that ERF scales linearly with concentration, microplastics in the combined fragments and fibres simulation yield a net ERF of 0.044 ± 0.399 mW m^{-2} when the global-mean surface concentration is 1 MP m^{-3}; approximately the median concentration from Fig. 1. Thus, the computed microplastic ERF for the present-day atmosphere is small compared with the total aerosol ERF[27] of between −0.71 and −0.14 W m^{-2}.

So far only one study has identified the presence of microplastics above the planetary boundary layer, with concentrations ranging between 13.9 MP m^{-3} above urban areas and 1.5 MP m^{-3} above rural areas, at altitudes up to 3.5 km above sea level[36]. Understanding the vertical distribution of microplastics is important as it influences radiative fluxes[37]. A sensitivity simulation with microplastics confined to the lowest 2 km of the GCM yields a net ERF of −0.746 ± 0.553 mW m^{-2} assuming a surface concentration of 1 MP m^{-3}. As can be seen in Fig. 3b, the longwave ERF is particularly sensitive to the vertical distribution of microplastics, as expected due to the decrease in temperature, pressure

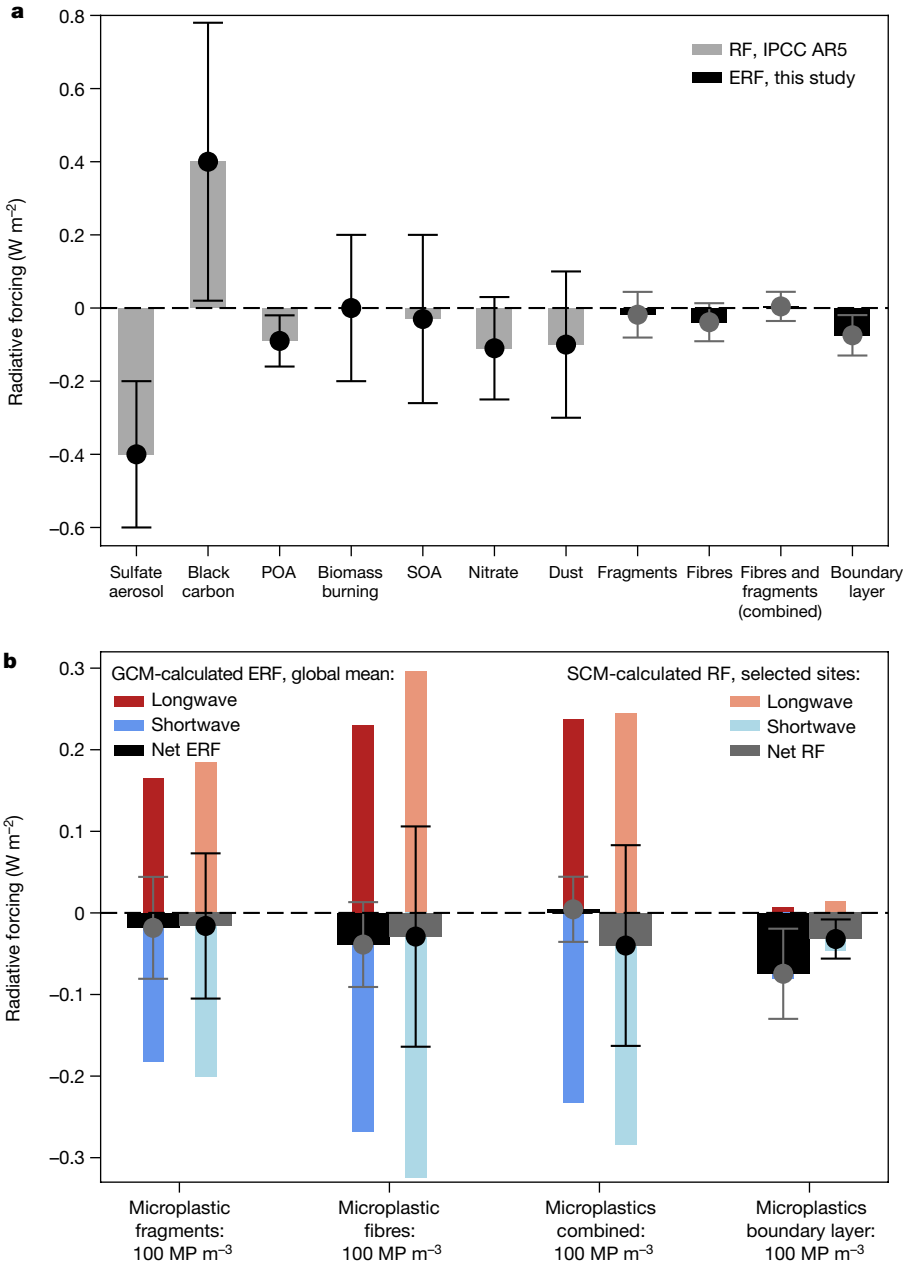

Fig. 3 | ERF of airborne microplastics. a, Global- and annual-mean clear-sky ERF values are shown for non-pigmented microplastics, averaged over 20-year GCM simulations for fragments, fibres and a combined fragments and fibres simulation. Microplastics are assumed to be present up to 10 km altitude with a surface concentration of 100 MP m^{-3}. Also shown is a simulation in which microplastics are assumed to be in the boundary layer only (bottom 2 km of the atmosphere), with a surface concentration of 100 MP m^{-3}. Error bars indicate the 90% confidence interval (see Methods). For comparison, the global- and annual-mean radiative forcing (RF) due to aerosol–radiation interactions between 1750 and 2011 of seven aerosol components are included (as listed in table 8.4 of IPCC AR5[26]). POA represents primary organic aerosol; SOA represents secondary organic aerosol. **b**, Global- and annual-mean microplastic ERF is shown as in **a**, along with longwave and shortwave ERF. Also shown are RF values calculated from a simple set of SCM simulations using fixed temperature profiles and clouds for selected geographical sites and solar zenith angles. Error bars on the SCM-calculated RF values represent the mean ± 1 s.d. Note the different *y* axis ranges in **a** and **b**.

and water vapour with altitude. The longwave ERF becomes disproportionately smaller when microplastics span 0–2 km altitude rather than 0–10 km, yielding a pronounced net negative ERF. Although the net ERF in the boundary layer experiment is still small compared with the total aerosol ERF, it demonstrates that if airborne microplastics are present only in the boundary layer, they will have a more substantial impact on surface climate than if they are distributed throughout the troposphere.

Finally, single-column model (SCM) simulations were performed for selected geographical sites and solar zenith angles (see Methods) to investigate how much of the microplastic ERF is due to radiative effects versus rapid adjustments (for example, changes in clouds[38]). From SCM simulations with microplastics prescribed up to 10 km altitude (with a surface concentration of 100 MP m^{-3} and vertical scaling applied, as in the GCM simulations), the mean radiative forcing was calculated over seven sets of atmospheric conditions (see Methods) with fixed cloud and temperature profiles. The mean radiative forcings are −0.016 ± 0.089, −0.029 ± 0.135, −0.040 ± 0.123 and −0.032 ± 0.024 W m^{-2} for the fragments, fibres, combined and boundary layer simulations, respectively (Fig. 3b). In comparison, the global-mean ERFs, calculated from the GCM and allowing all physical variables in the atmosphere to respond

to microplastics, are −0.018 ± 0.125, −0.039 ± 0.104, 0.004 ± 0.078 and −0.075 ± 0.111 W m^{-2} for the fragments, fibres, combined and boundary layer simulations, respectively. Because the SCM was run for only seven specific cases, the results are not definitive; however, the GCM-calculated ERFs and SCM-calculated radiative forcings are similar in magnitude and direction, which suggests that the microplastic ERF is not obscured by (or dominated by) rapid adjustments. Running the SCM for all solar zenith angles, latitudes and longitudes would allow a thorough investigation of the contribution of rapid adjustments to the total microplastic ERF and should be addressed in future studies.

Discussion and outlook

Further research is needed to constrain our estimate of microplastic ERF. First, more field studies across a range of urban and remote locations are needed to better understand the concentration of airborne microplastics—both in terms of the geographical and vertical distributions. The majority of the studies used to inform our estimate of microplastic surface concentrations were carried out in Europe and Asia (Fig. 1). Other types of anthropogenic aerosol, such as nitrate aerosol, tend to exhibit peak concentrations over Europe and East Asia[39] and thus the studies considered here may not reflect the global average accurately. On the other hand, many previous studies used micro-Fourier transform infrared spectroscopy, which cannot identify particles smaller than 11 μm. Particles in the 5–10 μm size range accounted for half of the microplastics present in studies using SEM-EDX[13] and Raman spectral imaging[12]. Owing to detection limits, these studies were not able to indicate whether nanoplastics were present; however, mass-based analysis methods suggest that they are[18]. Therefore, along with more studies being performed around the world, analytical methods must be improved and standardized such that we can measure airborne plastics accurately.

As already discussed, the microplastic ERF is highly sensitive to the vertical distribution of microplastics because longwave radiative effects depend on aerosol size, along with atmospheric conditions such as temperature. Future studies identifying whether microplastics are distributed throughout the troposphere are thus essential to constrain microplastic ERF.

The optical properties of microplastics calculated in this study were based on refractive indices of pure polymers (Extended Data Fig. 5), which were the only wavelength-dependent data available (see Methods). In reality, environmental microplastics have a wide range of colours—commonly black, grey and red (Extended Data Fig. 6). The colouring is typically achieved by mixing pure polymers with organic or inorganic pigments, which alter the colour of the polymer via their effect on the complex refractive index in the visible spectrum. Similarly, it is expected that they also change the refractive index of the material in the infrared spectrum. Plastics composed of the same polymer will therefore have variable refractive indices depending on the pigment and other potential additives found in the material, such as optical brighteners[40], along with any organic coatings they may have accumulated in the environment. It may be that pigmented microplastics are more absorbing than they are scattering in the visible spectrum, yield a net positive ERF and contribute to atmospheric warming, as previously suggested[25]. Further research is needed to assess the range of possible refractive indices when pigments are bound in polymers, and the resulting range of the microplastic ERF.

In calculating microplastic ERF, we considered only direct microplastic–radiation interactions. Atmospheric aerosols can influence cloud lifetime and albedo by acting as cloud condensation nuclei or ice nucleating particles[41,42]. Recent research indicates that nanoplastics are present in the atmosphere[18], and given their size range, may interact with clouds. Laboratory evidence suggests that, due to their hydrophobic nature, micro- and nanoplastics may act as cloud ice nuclei[43]; however, their contribution to cloud formation may depend on organic coatings accumulated in the environment and very little is known about this. Microplastic–cloud interactions may therefore be important too, especially in regions such as the Southern Ocean where clouds are highly sensitive to the concentration of ice nucleating particles[44]. Limited evidence suggests that microplastic concentrations over the remote ocean are low[15]; however, microplastics are abundant in the world's oceans[45] and may be co-emitted with sea spray[3]. Moreover, recent modelling suggests that continents receive more microplastics from mismanaged plastic waste in the oceans (via co-emission with sea spray and atmospheric transport) than they produce in a year[24].

In summary, we calculate the ERF of non-pigmented airborne microplastics to be 0.044 ± 0.399 mW m^{-2} assuming a global-mean surface concentration of 1 MP m^{-3} and present throughout the troposphere, or −0.746 ± 0.554 mW m^{-2} when confined to the atmospheric boundary layer. Uncertainties arise due to a current lack of data; the magnitude of ERF is influenced by the concentration of microplastics, and the sign is subject to uncertainties in the wavelength-dependent refractive index, which depends on properties such as composition and colour. Airborne microplastic pollution will become more severe in future—not only are microplastics durable but, based on current production and waste management trends, the abundance of plastic accumulated in landfills and the environment is projected to double over the next three decades[28]. Since plastic degrades through age and exposure to UV light to produce secondary microplastics, we expect microplastics to be present in Earth's atmosphere for many years to come. In the absence of serious efforts to address microplastic pollution, mismanaged plastic waste could exert an influence on climate in the future. Future research should assess whether microplastics influence climate regionally; anthropogenic aerosols have been linked to changes in heat extremes[46], and microplastics may similarly influence local and regional climate. This is especially true of urban environments, where airborne microplastics are already present on the order of hundreds to thousands of microplastic particles per cubic metre, and may already contribute locally to atmospheric heating and/or cooling.

Online content

Any methods, additional references, Nature Research reporting summaries, source data, extended data, supplementary information, acknowledgements, peer review information; details of author contributions and competing interests; and statements of data and code availability are available at https://doi.org/10.1038/s41586-021-03864-x.

1. Akhbarizadeh, R. et al. Suspended fine particulate matter ($PM_{2.5}$), microplastics (MPs), and polycyclic aromatic hydrocarbons (PAHs) in air: Their possible relationships and health implications. *Environ. Res.* **192**, 110339 (2021).
2. Allen, S. et al. Atmospheric transport and deposition of microplastics in a remote mountain catchment. *Nat. Geosci.* **12**, 339–344 (2019).
3. Allen, S. et al. Examination of the ocean as a source for atmospheric microplastics. *PLoS ONE* **15**, e0232746 (2020).
4. Bergmann, M. et al. White and wonderful? Microplastics prevail in snow from the Alps to the Arctic. *Sci. Adv.* **5**, eaax1157 (2019).
5. Brahney, J., Hallerud, M., Heim, E., Hahnenberger, M. & Sukumaran, S. Plastic rain in protected areas of the United States. *Science* **368**, 1257–1260 (2020).
6. Cai, L. et al. Characteristic of microplastics in the atmospheric fallout from Dongguan city, China: preliminary research and first evidence. *Environ. Sci. Pollut. Res. Int.* **24**, 24928–24935 (2017).
7. Dris, R., Gasperi, J., Saad, M., Mirande, C. & Tassin, B. Synthetic fibers in atmospheric fallout: a source of microplastics in the environment? *Mar. Pollut. Bull.* **104**, 290–293 (2016).
8. Dris, R. et al. A first overview of textile fibers, including microplastics, in indoor and outdoor environments. *Environ. Pollut.* **221**, 453–458 (2017).
9. Gaston, E., Woo, M., Steele, C., Sukumaran, S. & Anderson, S. Microplastics differ between indoor and outdoor air masses: insights from multiple microscopy methodologies. *Appl. Spectrosc.* **74**, 1079–1098 (2020).
10. Klein, M. & Fischer, E. K. Microplastic abundance in atmospheric deposition within the metropolitan area of Hamburg, Germany. *Sci. Total Environ.* **685**, 96–103 (2019).
11. Knobloch, E. et al. Comparison of deposition sampling methods to collect airborne microplastics in Christchurch, New Zealand. *Wat. Air Soil Pollut.* **232**, 133 (2021).
12. Levermore, J. M., Smith, T. E. L., Kelly, F. J. & Wright, S. L. Detection of microplastics in ambient particulate matter using Raman spectral imaging and chemometric analysis. *Anal. Chem.* **92**, 8732–8740 (2020).
13. Li, Y. et al. Airborne fiber particles: types, size and concentration observed in Beijing. *Sci. Total Environ.* **705**, 135967 (2020).

14. Liu, K. et al. Source and potential risk assessment of suspended atmospheric microplastics in Shanghai. *Sci. Total Environ.* **675**, 462–471 (2019).
15. Liu, K. et al. Consistent transport of terrestrial microplastics to the ocean through atmosphere. *Environ. Sci. Technol.* **53**, 10612–10619 (2019).
16. Liu, C. et al. Widespread distribution of PET and PC microplastics in dust in urban China and their estimated human exposure. *Environ. Int.* **128**, 116–124 (2019).
17. Liu, K. et al. Global inventory of atmospheric fibrous microplastics input into the ocean: an implication from the indoor origin. *J. Hazard. Mater.* **400**, 123223 (2020).
18. Materić, D. et al. Micro- and nanoplastics in Alpine snow: a new method for chemical identification and (semi)quantification in the nanogram range. *Environ. Sci. Technol.* **54**, 2353–2359 (2020).
19. Su, L., Nan, B., Craig, N. J. & Pettigrove, V. Temporal and spatial variations of microplastics in roadside dust from rural and urban Victoria, Australia: implications for diffuse pollution. *Chemosphere* **252**, 126567 (2020).
20. Syafei, A. D., Nurasrin, N. R., Assomadi, A. F. & Boedisantoso, R. Microplastic pollution in the ambient air of Surabaya, Indonesia. *Curr. World Environ.* **61**, 290–298 (2019).
21. Wang, X. et al. Atmospheric microplastic over the South China Sea and East Indian Ocean: abundance, distribution and source. *J. Hazard. Mater.* **389**, 121846 (2020).
22. Wright, S. L., Ulke, J., Font, A., Chan, K. L. A. & Kelly, F. J. Atmospheric microplastic deposition in an urban environment and an evaluation of transport. *Environ. Int.* **136**, 105411 (2020).
23. Zhang, Y. et al. Microplastics in glaciers of the Tibetan Plateau: evidence for the long-range transport of microplastics. *Sci. Total Environ.* **758**, 143634 (2021).
24. Brahney, J. et al. Constraining the atmospheric limb of the plastic cycle. *Proc. Natl Acad. Sci. USA* **118**, e2020719118 (2021).
25. Evangeliou, N. et al. Atmospheric transport is a major pathway of microplastics to remote regions. *Nat. Commun.* **11**, 3381 (2020).
26. Myhre, G. et al. in *Climate Change 2013: The Physical Science Basis* (eds Stocker, T. F. et al.) Ch. 8 (IPCC, Cambridge Univ. Press, 2013).
27. Bellouin, N. et al. Bounding global aerosol radiative forcing of climate change. *Rev. Geophys.* **58**, e2019RG000660 (2020).
28. Geyer, R., Jambeck, J. R. & Law, K. L. Production, use, and fate of all plastics ever made. *Sci. Adv.* **3**, e1700782 (2017).
29. Andrady, A. L. Microplastics in the marine environment. *Mar. Pollut. Bull.* **62**, 1596–1605 (2011).
30. de Souza Machado, A. A., Kloas, W., Zarfl, C., Hempel, S. & Rillig, M. C. Microplastics as an emerging threat to terrestrial ecosystems. *Glob. Change Biol.* **24**, 1405–1416 (2018).
31. Rochman, C. M. Microplastics research—from sink to source. *Science* **360**, 28–29 (2018).
32. Goodman, K. E., Hare, J. T., Khamis, Z. I., Hua, T. & Sang, Q.-X. A. Exposure of human lung cells to polystyrene microplastics significantly retards cell proliferation and triggers morphological changes. *Chem. Res. Toxicol.* **34**, 1069–1081 (2021).
33. Spracklen, D. V. et al. Explaining global surface aerosol number concentrations in terms of primary emissions and particle formation. *Atmos. Chem. Phys.* **10**, 4775–4793 (2010).
34. Bullard, J. E., Ockelford, A., O'Brien, P. & McKenna Neuman, C. Preferential transport of microplastics by wind. *Atmos. Environ.* **245**, 118038 (2021).
35. Tsigaridis, K. & Kanakidou, M. The Present and future of secondary organic aerosol direct forcing on climate. *Curr. Clim. Change Rep.* **4**, 84–98 (2018).
36. González-Pleiter, M. et al. Occurrence and transport of microplastics sampled within and above the planetary boundary layer. *Sci. Total Environ.* **761**, 143213 (2020).
37. Mishra, A. K., Koren, I. & Rudich, Y. Effect of aerosol vertical distribution on aerosol-radiation interaction: a theoretical prospect. *Heliyon* **1**, e00036 (2015).
38. Lohmann, U. et al. Total aerosol effect: radiative forcing or radiative flux perturbation? *Atmos. Chem. Phys.* **10**, 3235–3246 (2010).
39. Bellouin, N. et al. Aerosol forcing in the Climate Model Intercomparison Project (CMIP5) simulations by HadGEM2-ES and the role of ammonium nitrate. *J. Geophys. Res.* **116**, D20206 (2011).
40. Jervis, D. A. Optical brighteners: improving the colour of plastics. *Plast. Addit. Compd* **5**, 42–46 (2003).
41. Twomey, S. The influence of pollution on the shortwave albedo of clouds. *J. Atmos. Sci.* **34**, 1149–1152 (1977).
42. Albrecht, B. A. Aerosols, cloud microphysics, and fractional cloudiness. *Science* **245**, 1227–1230 (1989).
43. Ganguly, M. & Ariya, P. A. Ice Nucleation of model nanoplastics and microplastics: a novel synthetic protocol and the influence of particle capping at diverse atmospheric environments. *ACS Earth Space Chem.* **3**, 1729–1739 (2019).
44. Vergara-Temprado, J. et al. Strong control of Southern Ocean cloud reflectivity by ice-nucleating particles. *Proc. Natl Acad. Sci. USA* **115**, 2687–2692 (2018).
45. Eriksen, M. et al. Plastic pollution in the world's oceans: more than 5 trillion plastic pieces weighing over 250,000 tons afloat at sea. *PLoS ONE* **9**, e111913 (2014).
46. Boé, J., Somot, S., Corre, L. & Nabat, P. Large discrepancies in summer climate change over Europe as projected by global and regional climate models: causes and consequences. *Clim. Dyn.* **54**, 2981–3002 (2020).
47. Wessel, P. & Smith, W. H. F. A global self-consistent, hierarchical, high-resolution shoreline database. *J. Geophys. Res. Solid Earth* **101**, 8741–8743 (1996).
48. *Python Language Reference, Version 3.6* https://www.python.org/downloads/release/python-360/ (Python Software Foundation).

Methods

Empirical properties of airborne microplastics

Morphotype. Microplastics are typically categorized as fragments, fibres and films according to their morphotype. Because the shape of a particle affects how it scatters and absorbs radiation, it is important to take morphotype into account when calculating optical properties. Morphotypes reported by eight studies are summarized in Extended Data Fig. 4. For simplicity, granules were included in the same group as fragments. The median occurrences of fibres, fragments and films were approximately 60%, 35% and 20%, respectively (not normalized to unity). Since films are less common than other morphotypes and little is known about their size distribution, they were excluded from further analysis. In carrying out our assessment of the combined ERF of microplastic fragments and fibres, we approximated their median occurrences to assume a combination of 50% fragments and 50% fibres (Extended Data Table 1).

Size distribution and aspect ratio. Size distributions of airborne microplastic fibres and fragments are approximated by gamma distributions in Extended Data Figs. 2, 3. Fragment diameters peak at approximately 10 μm whereas fibre lengths peak at approximately 200 μm. Fibres are characterized by their length and diameter. In reality they also occur in curved shapes, but considering the uncertainties involved in our other assumptions, we do not expect this to be a limiting factor in the accuracy of the ERF calculations. Extended Data Fig. 7 shows the empirical aspect ratio of fibres[4]. To simplify the result, we approximated the relationship between the fibre length L and diameter D by fitting a logarithmic curve of the form:

$$D = A \log\left(1 + \frac{L}{B}\right) \quad (1)$$

where A = 6 μm and B = 30 μm are coefficients determined using the least squares method, and rounded to the nearest integer.

Refractive index. The optical properties of materials depend on the (dimensionless) refractive index as a function of wavelength. Refractive indices of pure polymers are shown in Extended Data Fig. 5 (refs. [49–55]). Owing to the similarities in the wavelength-dependent refractive indices of different polymers and the lack of data for all polymer types, we approximated the refractive index of airborne microplastics with an empirical, analytical average form. For the real part, n, (responsible for refraction) we used a one-term Sellmeier model[56]:

$$n = \left(1 + \frac{a\lambda^2}{\lambda^2 - b^2}\right)^{\frac{1}{2}} \quad (2)$$

where λ is the wavelength and a and b are determined by least squares optimization. The coefficients were determined to be a = 1.4 and $b = 1.1 \times 10^{-7}$ m. For the imaginary part k (which determines the absorption coefficient), we fitted a fourth-degree polynomial by least squares optimization between 0.4 μm and 100 μm:

$$\log_{10}(k) = c_0 + c_1 x + c_2 x^2 + c_3 x^3 + c_4 x^4 \quad (3)$$

x is the $\log_{10}$ of the wavelength in metres, and the coefficients were determined to be $c_0 = 550$, $c_1 = 460$, $c_2 = 140$, $c_3 = 19$ and $c_4 = 0.93$. As k is much smaller than n, this polynomial approximation remains compatible with the Kramers–Krönig relations.

Colour and composition. Due to the lack of measurements of optical properties of coloured plastics, we did not account for different colours in our refractive index models. Future research should assess the impact of colour on microplastic ERF and we therefore include colour and composition information here for completeness. The colour of atmospheric microplastics based on six studies is summarized in Extended Data Fig. 6. The most commonly reported colour was black (including grey; median occurrence 30%) followed by red (median occurrence 23%), white (including transparent), yellow and blue (median occurrence ~12% each).

Microplastics can be broadly characterized as synthetic (for example polyethylene and polypropylene) or semi-synthetic (such as rayon, viscose or cellophane)[57]. Here we assess the impact of synthetic microplastics, which are generally non-biodegradable (unlike semi-synthetic plastics) and therefore more likely to be widespread in the environment. Previous studies reported a mixture of synthetic, semi-synthetic and natural fibres since natural fibres may contain toxic dyes that could yield similar harmful effects on the environment as synthetic fibres[6,7]. Extended Data Fig. 1 shows the composition of environmental fragments and fibres. Fragments were mostly resins and polyethylene and polypropylene (median occurrence ~25% each). Fibres were predominantly polyester (median occurrence 80%), probably originating from synthetic textiles, followed by polyethylene and polypropylene (median occurrence 20%), with a smaller contribution of acrylic, polyamide (including nylon) and polyurethane (median occurrence ~10% each). The reported microplastic compositions compare reasonably well with the production data reported for the European and Asian markets, which is where the majority of studies summarized in Fig. 1 were performed. In Europe and Asia, the most commonly produced polymers are polypropylene, polyethylene and polyvinyl chloride[58,59].

Calculation of microplastic optical properties

Fragments. We assumed that fragments are approximately spherical and calculated their scattering and absorption efficiencies and asymmetry factors using Mie theory. Calculations were performed with the Suite of Community Radiative Transfer codes based on Edwards and Slingo (SOCRATES)[60]. Mie scattering and absorption cross-sections, single-scattering albedos and asymmetry factors of spherical fragments calculated with a fitted refractive index and assuming a gamma size distribution are shown in Fig. 2. The optical parameters were weighted by the incoming solar spectrum[61] to calculate integral properties in each spectral band. The integral properties were then used to prepare volume scattering and absorption coefficients and asymmetry factors for the GCM by multiplying by the number concentration (in MP m^{-3}) of fragments (Extended Data Table 2).

Fibres. We assumed that the fibres' lengths were distributed as a gamma distribution with a shape parameter of 2.5, and a scale parameter of 250 μm as in Extended Data Fig. 3, for L = 10–2,500 μm. The diameter D of the fibres was assumed to follow equation (1). Fibres were considered to be cylinders of length $L - D$, with a hemispherical cap at each end to give a total length of L. Because fibres have typically large size parameters $L/\lambda \gg 1$, we used a combination of geometric ray-tracing and the extinction paradox to estimate the scattering properties[62]. This gives the orientation-averaged extinction cross-section as $\langle C_{ext} \rangle = S/2$, where S is the surface area[63]. The absorption cross-section is estimated by the method of Kokhanovsky and Macke[64], which itself is an extension of Bohren and Huffman[65]. This expresses the orientation-averaged absorption cross section as:

$$\langle C_{abs} \rangle = \frac{S}{4} [1 - R(n)][1 - e^{-\psi(n)c(k)}] \quad (4)$$

where $R(n)$ is the reflectance of Lambertian light from an interface[66], $\psi(n) = \frac{2\phi(n)}{3(1 - R(n))}$, $\phi(n)$ is the mean path length of rays incident on the object, and $c(k) = 3V\alpha(k)/(2S)$ for a fibre with volume V and surface area S, and $\alpha(k) = 4\pi k/\lambda$ is the absorption coefficient. Ray-tracing simulations were used to obtain $\phi(n)$. The orientation-averaged scattering cross-section is then obtained as $\langle C_{sca} \rangle = \langle C_{ext} \rangle - \langle C_{abs} \rangle$.

The asymmetry factor g is obtained following Kokhanovsky and Macke[64] as:

$$g = g_\infty(n) - [g_\infty(n) - g_0(n)] \exp(-\beta(n)c(k)) \quad (5)$$

$c(k)$ was defined earlier and is the only parameter that depends on the absorption coefficient (but not on n). g_∞ is the asymmetry factor at high absorption—it depends on the refractive index n but is independent of shape for randomly oriented objects and therefore we can use the known analytic expression for a sphere[62]. g_0 is the asymmetry factor at zero absorption and depends on the shape (but not size) and refractive index of the object. We calculate it from ray-tracing simulations. $\beta(n)$ also depends on the shape (not size) and n. For a given shape and n, we can derive β by calculating g in a single ray-tracing simulation in the low-absorbing case (we used $c(k) = 3.75 \times 10^{-4}$) and inverting equation (5) in this limit:

$$\beta \equiv \frac{g - g_0}{(g_\infty(n) - g_0)\, c} \quad (6)$$

The properties that are extracted from ray tracing (g_0 and β) were calculated on a grid of seven linearly spaced refractive indices from 1.5 to 1.8, and 50 shapes with aspect ratios from 1 to 200, spaced on a log scale. Values used in the calculations were then linearly interpolated from these data. The ray-tracing simulations used 10^7 rays incident on each object.

As was done for fragments, fibre optical parameters were weighted by the incoming solar spectrum[61] to calculate integral properties in each spectral band. These were then used to prepare volume-scattering and absorption coefficients and asymmetry factors as an input to the GCM by multiplying by the number concentration of fibres. Extended Data Table 2 contains the fibre optical properties input to the GCM.

Modelling direct radiative effects

HadGEM3 general circulation model. To assess the effect of airborne microplastics on the global energy balance, we performed simulations with the Hadley Centre Global Environment Model version 3–Global Atmosphere model 7.1 (HadGEM3-GA7.1)[67], developed by the UK Met Office and the Unified Model Partnership. The model uses a regular longitude–latitude 1.875° × 1.25° grid with 85 vertical levels between the surface and 85 km altitude, and the radiative transfer scheme SOCRATES[60]. The radiative transfer scheme divides the shortwave part of the spectrum between 200 nm and 10 μm into six spectral bands and the longwave part between 3.3 μm and 1 cm into nine spectral bands.

We used HadGEM3's EasyAerosol scheme[68] to supply the radiative transfer code with a five-dimensional (longitude × latitude × level × spectral band × time) grid of volume scattering and absorption coefficients and asymmetry factors calculated for the given concentration and optical properties of microplastics. The absorption and scattering coefficients of microplastics were added to the model's coefficients calculated for atmospheric gases, aerosols and clouds. We considered only direct aerosol–radiation interactions in calculating microplastic ERF, since little is known regarding whether microplastics play a role in indirect aerosol effects on cloud lifetime and albedo.

Due to the current lack of globally distributed and vertically resolved measurements, we assume that airborne microplastics are distributed uniformly over the Earth. While previous studies indicate that the distribution is not uniform (Fig. 1), too few measurements are available—particularly from the Southern Hemisphere—to derive a global distribution. Prescribing a uniform concentration allows us to obtain a conservative first estimate of microplastic ERF.

Aside from a recent series of aircraft flights that identified microplastic concentrations of up to 20 MP m^{-3} above the planetary boundary layer[37], little is known about the vertical distribution of microplastic, including the maximum altitude at which they may be found. We have assumed that microplastics are most abundant at the surface and that their concentration decreases with altitude. We prescribed a vertical distribution of microplastics in the model assuming that the concentration decreases to 0.3 of the surface concentration at 10 km above sea level, since air density at 10 km altitude is approximately 0.3 of the surface air density. The vertical distribution of microplastics was calculated as:

$$[\mathrm{MP}]_z = 0.3^{\frac{z}{10}} \quad (7)$$

where z is the altitude in kilometres above sea level and $[\mathrm{MP}]_z$ is the microplastic concentration at that altitude. We assumed that microplastics are not transported into the stratosphere, and thus set the microplastic concentration above 10 km (the approximate height of the tropopause) to zero.

To test our assumptions regarding vertical distribution, we performed a sensitivity simulation in which microplastics were confined to the lowest 2 km of the atmosphere (the approximate height of the boundary layer). The vertical distribution was computed using equation (7), and the microplastic concentration above 2 km was set to zero.

Simulations and calculation of ERF. Five simulations were performed, each 20 yr in duration from 1990–2009 (Extended Data Table 1). Sea surface temperatures, sea-ice concentrations and greenhouse gas concentrations were prescribed based on observations and aerosol emissions were taken from the CMIP5 database[69]. Microplastic surface concentrations were prescribed as in Extended Data Table 1, that is, with 100× scaling applied. This was done to clearly isolate signal from noise, under the assumption that ERF scales linearly with concentration. ERF is defined here as the difference in the global-mean net top-of-atmosphere radiation flux between simulations with and without microplastics[70].

We derived confidence intervals for the net ERF as follows. We calculated $N = 20$ annual geographical means from daily mean values of the top-of-atmosphere flux for the experimental and control runs, resulting in two vectors $\mathbf{X}_{\mathrm{exp}}$ and $\mathbf{X}_{\mathrm{cnt}}$ of length N, respectively. The geographical mean was weighted by the surface area of grid cells. We assumed that the annual means are approximately statistically independent between years and normally distributed. Next, we calculated the difference between the experimental and control run, $\mathbf{X} = \mathbf{X}_{\mathrm{exp}} - \mathbf{X}_{\mathrm{cnt}}$. From these 20 $\mathbf{X}$ values, we calculated the mean $\overline{\mathbf{X}}$ and standard deviation s. The distribution of the long-term (20-yr) difference between the experimental and control run is then t-distributed (that is, similar to a normal distribution but with heavier tails) with $N - 1$ degrees of freedom, a shift of $\overline{\mathbf{X}}$ and scale of $s/\sqrt{N}$. Lastly, we calculated the 90% confidence interval as the 5th to 95th percentiles of this t-distribution.

SCM. To assess the effect of atmospheric microplastics on radiative transfer, ignoring rapid adjustments induced by microplastics (for example, changes in clouds), we performed simulations with an SCM. We applied SOCRATES on the Continual Intercomparison of Radiation Codes (CIRC) cases[71], which provide thermodynamic, cloud and aerosol profiles based on observations along with reference measured and calculated radiative fluxes. The SCM consisted of only the radiative transfer code and did not simulate dynamics or physics. Holding atmospheric temperature, pressure and composition profiles, surface temperature, albedo and clouds fixed in the SCM allowed us to quantify the radiative effect of microplastics in these simple scenarios without rapid adjustments. We ran the SOCRATES code with the unmodified CIRC profiles (control simulations). For each CIRC case, we also ran the code with prescribed microplastics as in the GCM simulations (that is, with a surface concentration of 100 MP m^{-3} and vertical scaling applied; Extended Data Table 1). Radiative flux differences were calculated for each simulation relative to the control simulation.

Data availability

GCM data that support the findings of this study are available at https://doi.org/10.5281/zenodo.5093843. Source data are provided with this paper.

Code availability

Custom code generated in this study is available at https://doi.org/10.5281/zenodo.5093843.

49. Horwitz, J. W. Infrared refractive index of polyethylene and a polyethylene-based material. *Opt. Eng.* **50**, 093603 (2011).
50. Smith, D. R. & Loewenstein, E. V. Optical constants of far infrared materials. 3: plastics. *Appl. Opt.* **14**, 1335–1341 (1975).
51. Sultanova, N., Kasarova, S. & Nikolov, I. Dispersion Properties of Optical Polymers. *Acta Phys. Pol. A* **116**, 585–587 (2009).
52. Zhang, X., Qiu, J., Zhao, J., Li, X. & Liu, L. Complex refractive indices measurements of polymers in infrared bands. *J. Quant. Spectrosc. Radiat. Transf.* **252**, 107063 (2020).
53. Zhang, X., Qiu, J., Li, X., Zhao, J. & Liu, L. Complex refractive indices measurements of polymers in visible and near-infrared bands. *Appl. Opt.* **59**, 2337–2344 (2020).
54. Flores-Mijangos, J. & Beltrán-López, V. Far-infrared laser measurement of the refractive index of polypropylene. *Appl. Opt.* **42**, 592–596 (2003).
55. Myers, T. L. et al. Accurate measurement of the optical constants n and k for a series of 57 inorganic and organic liquids for optical modeling and detection. *Appl. Spectrosc.* **72**, 535–550 (2018).
56. Sellmeier, W. Ueber die durch die Aetherschwingungen erregten Mitschwingungen der Körpertheilchen und deren Rückwirkung auf die ersteren, besonders zur Erklärung der Dispersion und ihrer Anomalien. *Ann. Phys.* **223**, 386–403 (1872).
57. Kroon, F. J., Motti, C. E., Jensen, L. H. & Berry, K. L. E. Classification of marine microdebris: a review and case study on fish from the Great Barrier Reef, Australia. *Sci. Rep.* **8**, 16422 (2018).
58. *Plastics—The Facts 2018: An Analysis of European Plastics Production, Demand and Waste Data* (PlasticsEurope, 2018); http://www.plasticseurope.org
59. *China Leads in Growth of Polymers & Plastic Products*, (Plastemart, 2006); www.plastemart.com/upload/Literature/chineseplasticandpolymergrowth.asp
60. Edwards, J. M. & Slingo, A. Studies with a flexible new radiation code. I: choosing a configuration for a large-scale model. *Q. J. R. Meteorol. Soc.* **122**, 689–719 (1996).
61. Lean, J. L. & DeLand, M. T. How does the Sun's spectrum vary? *J. Clim.* **25**, 2555–2560 (2012).
62. Kokhanovsky, A. A. & Zege, E. P. Local optical parameters of spherical polydispersions: simple approximations. *Appl. Opt.* **34**, 5513–5519 (1995).
63. van de Hulst, H. C. *Light Scattering by Small Particles* (Wiley, 1957).
64. Kokhanovsky, A. A. & Macke, A. Integral light-scattering and absorption characteristics of large, nonspherical particles. *Appl. Opt.* **36**, 8785–8790 (1997).
65. Bohren, C. F. & Huffman, D. R. *Absorption and Scattering of Light by Small Particles* (John Wiley & Sons Inc., 1983).
66. Duntley, S. Q. The optical properties of diffusing materials. *J. Opt. Soc. Am.* **32**, 61–70 (1942).
67. Walters, D. et al. The Met Office Unified Model Global Atmosphere 7.0/7.1 and JULES Global Land 7.0 configurations. *Geosci. Model Dev.* **12**, 1909–1963 (2019).
68. Edwards, J. M., Manners, J., Thelen, J.-C., Ingram, W. J. & Hill, P. G. *Unified Model Documentation Paper 023: The Radiation Code (UM Version 11.4)* (Met Office, 2018).
69. Lamarque, J. F. et al. Historical (1850–2000) gridded anthropogenic and biomass burning emissions of reactive gases and aerosols: methodology and application. *Atmos. Chem. Phys.* **10**, 7017–7039 (2010).
70. Forster, P. M. et al. Recommendations for diagnosing effective radiative forcing from climate models for CMIP6. *J. Geophys. Res. Atmos.* **121**, 12460–12475, (2016).
71. Oreopoulos, L. & Mlawer, E. Modeling: the Continual Intercomparison of Radiation Codes (CIRC). *Bull. Am. Meteorol. Soc.* **91**, 305–310 (2010).

Acknowledgements This research was supported by the Royal Society of New Zealand Marsden Fund (contract number MFP-UOC1903). We acknowledge the UK Met Office for the use of the MetUM, SOCRATES and the Continual Intercomparison of Radiation Codes (CIRC). We acknowledge the contribution of New Zealand eScience Infrastructure (NeSI) high-performance computing facilities to the results of this research. New Zealand's national facilities are provided by NeSI and funded jointly by NeSI's collaborator institutions and through the Ministry of Business, Innovation and Employment's Research Infrastructure programme (https://www.nesi.org.nz, last access: 20 April 2021). We also acknowledge the use of the Rāpoi computing facility at Victoria University of Wellington, along with the open source software used in the analysis: Devuan GNU+Linux, Python, numpy, scipy and matplotlib. L.E.R. thanks Jonny Williams for technical assistance. L.E.R. and P.K. acknowledge R. Martinez Gazoni for helpful discussions.

Author contributions L.E.R. Conceptualized the study, acquired funding, supervised the study, wrote the original draft and conducted the analysis together with P.K. and W.R.C.S. . P.K. contributed to the methodology, software, validation, and writing of the original draft. E.C.L.R. contributed to the methodology, validation, funding acquisition, supervision and review and editing of the manuscript. W.R.C.S. contributed to the methodology and validation, and writing of the original draft. S.G. reviewed and edited the manuscript and contributed to funding acquisition.

Competing interests The authors declare no competing interests.

Additional information

Supplementary information The online version contains supplementary material available at https://doi.org/10.1038/s41586-021-03864-x.

Correspondence and requests for materials should be addressed to Laura E. Revell.

Peer review information *Nature* thanks Ben Booth, Steven Allen, Rachid Dris and the other, anonymous, reviewer(s) for their contribution to the peer review of this work.

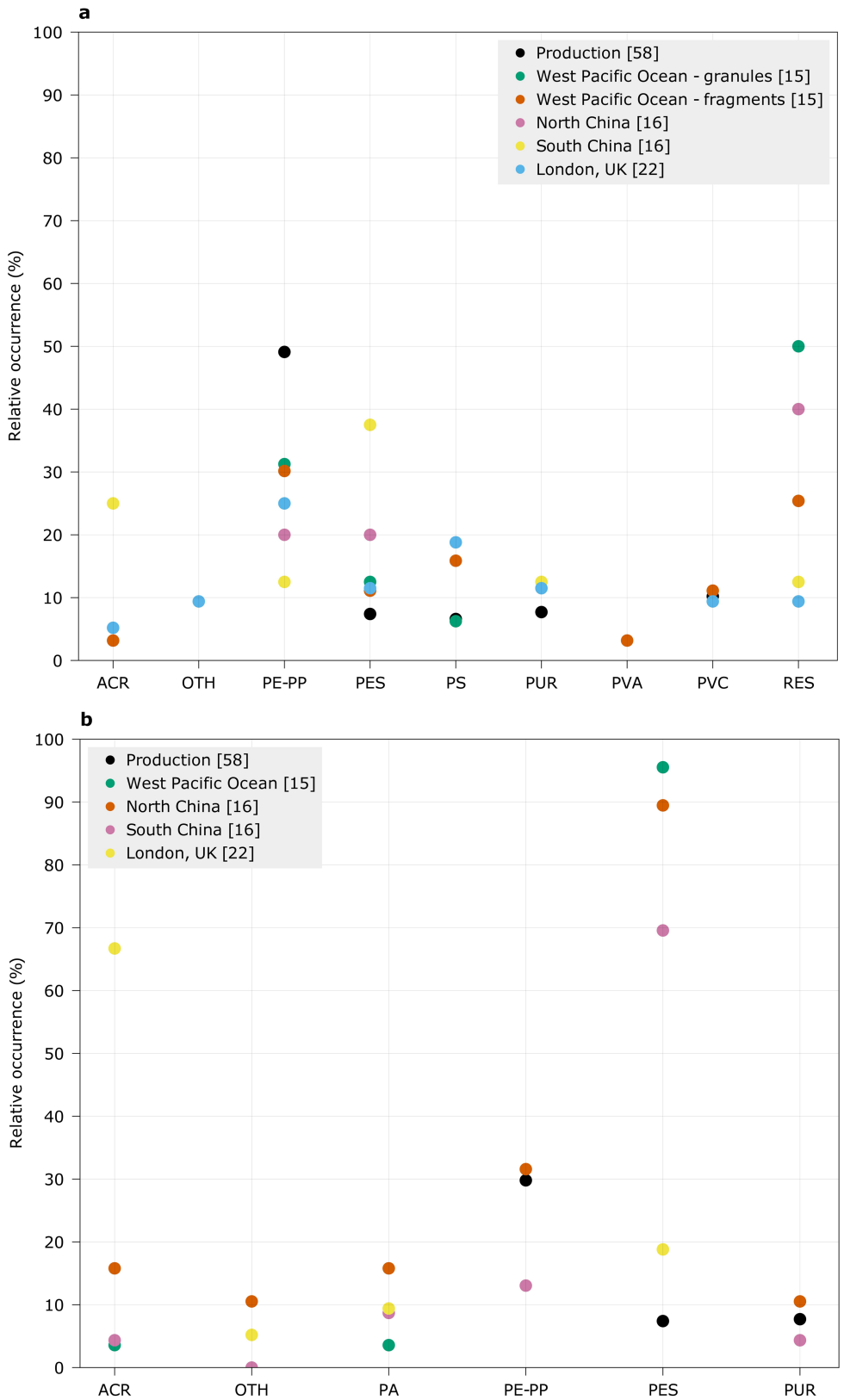

Extended Data Fig. 1 | Composition of airborne microplastics collected in previous studies compared with reported plastic production data. The studies included disaggregated composition by morphotype and are presented for (**a**) fragments; (**b**) fibres. Polymer compositions include acrylic (ACR, including polyacrylonitrile and poly(N-methyl acrylamide)), polyamide (PA, including nylon), polyethylene and polypropylene (PE-PP), polyester (PES, including polyethylene terephthalate), polystyrene (PS), polyurethane (PUR), polyvinyl acetate (PVA), polyvinyl chloride (PVC), resins (RES, including epoxy, phenoxy and alkyd resins), and various other types (OTH).

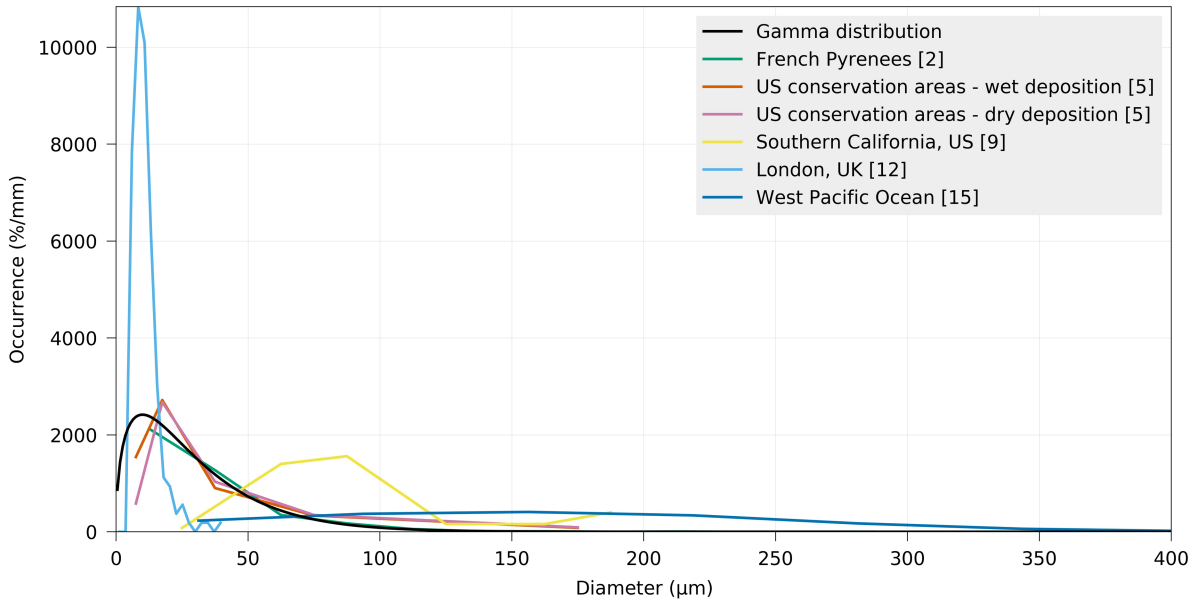

Extended Data Fig. 2 | Size distributions of microplastic fragments reported by previous studies. A gamma distribution was fitted to match the majority of the empirical distributions. The distributions are normalized to unity and approximated by a gamma distribution with the shape parameter of 2 and scale parameter 15 µm.

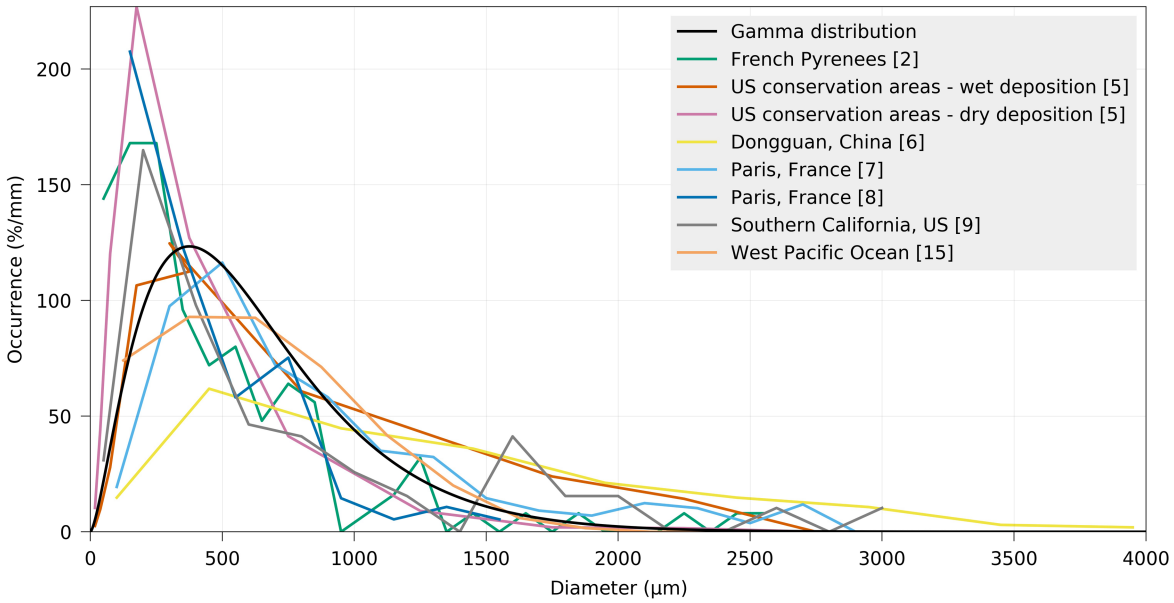

Extended Data Fig. 3 | Size distributions of microplastic fibre lengths reported by previous studies. A gamma distribution was fitted to match the majority of the empirical distributions. The distributions are normalized to unity and approximated by a gamma distribution with the shape parameter of 2.5 and scale parameter 250 µm.

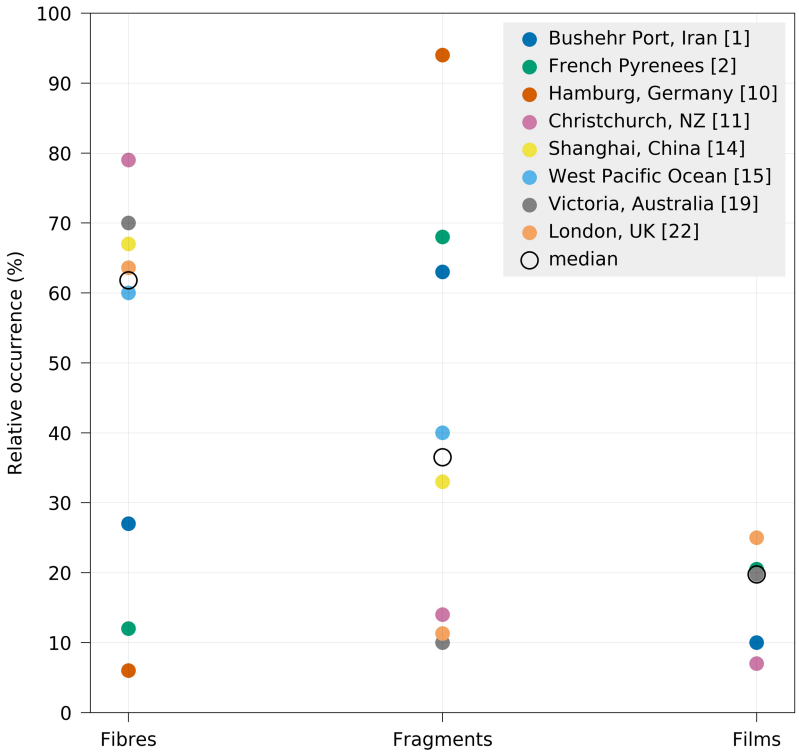

Extended Data Fig. 4 | Morphotypes of airborne microplastic collected in previous studies.

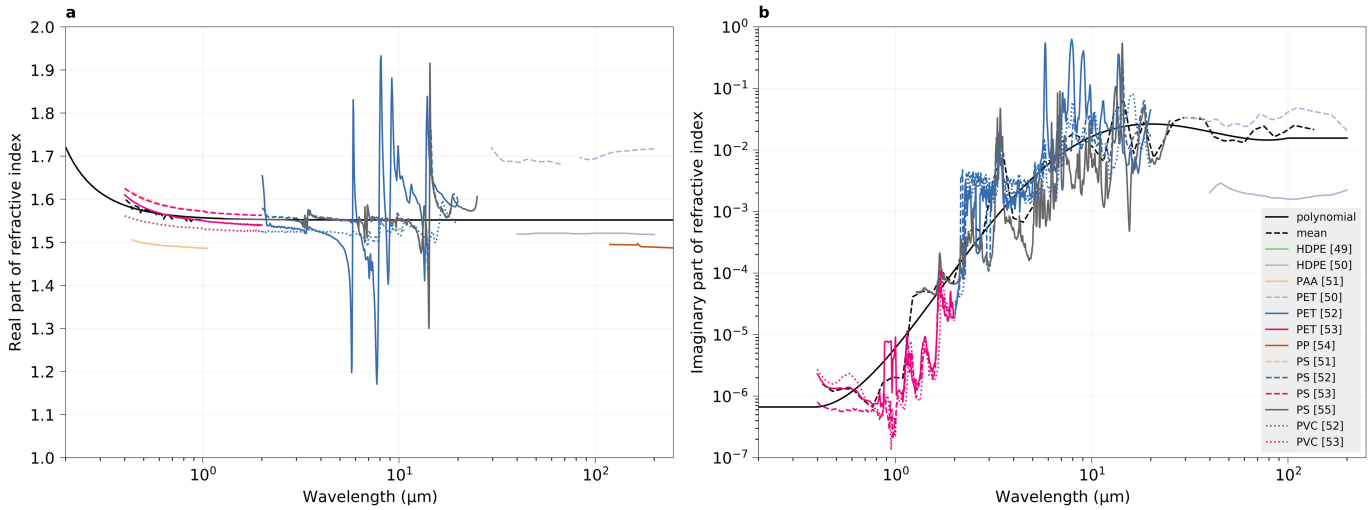

Extended Data Fig. 5 | Refractive index of polymers based on a literature survey. Polymer compositions include high-density polyethylene (HDPE), polyacrylic acid (PAA), polyethylene terephthalate (PET), polypropylene (PP), polystyrene (PS) and polyvinyl chloride (PVC). The mean calculated over regular wavelength intervals on a $\log_{10}$ scale is shown by the dashed black lines. In (a) equation (2) was fitted to the mean. In (b) equation (3) was used to fit a 4^{th} degree polynomial to the $\log_{10}$ of the mean using the least squares method. The solid black lines represent the fits given by equations (2) and 3, and these fits were used in the calculations of microplastic optical properties.

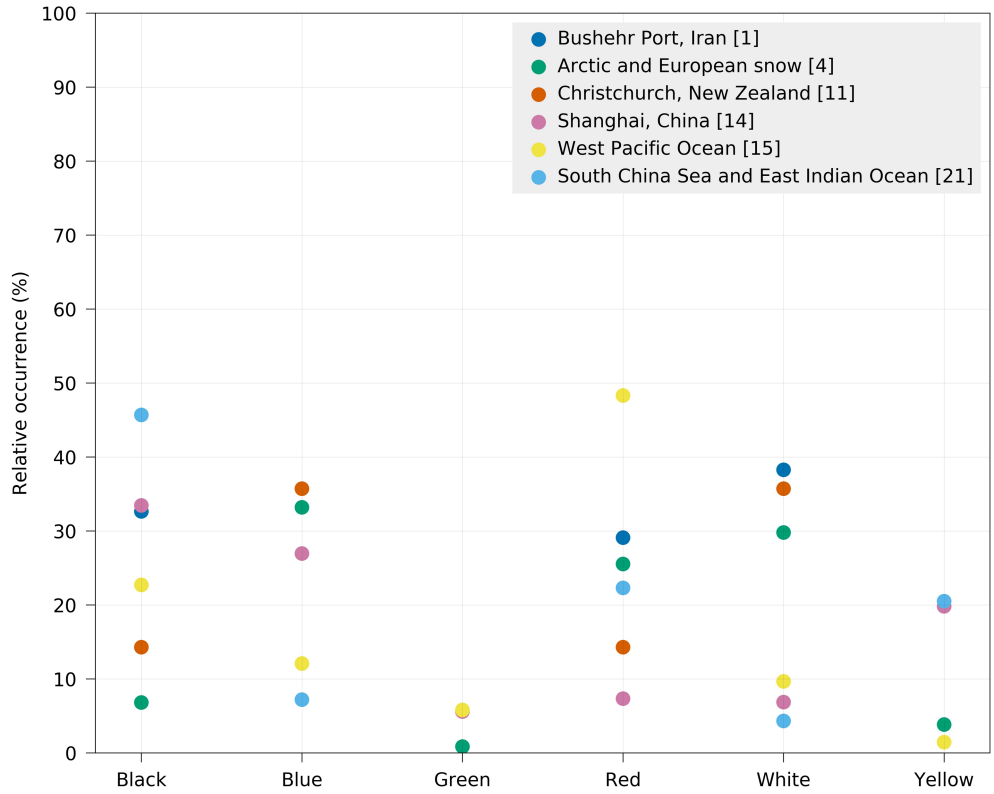

Extended Data Fig. 6 | Colours of airborne microplastics collected in previous studies, where colour was reported. Black includes grey; blue includes turquoise; green includes lime; red includes pink, purple, brown and orange; white includes transparent.

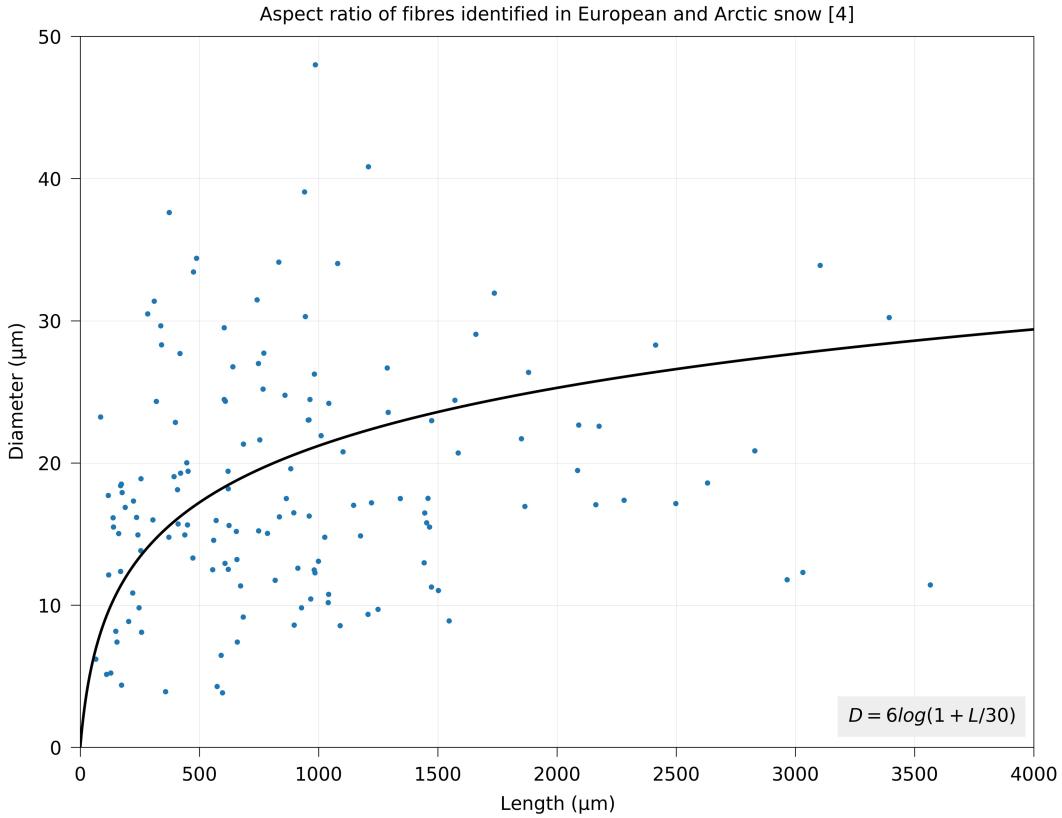

Extended Data Fig. 7 | The empirical aspect ratio of fibres collected in European and Arctic snow (the only study to date to report fibre aspect ratio). A least squares fit of the form $D = A \log\left(1 + \frac{L}{B}\right)$ is also shown, where D is the fibre diameter, L is the fibre length and A and B are fitted coefficients, rounded to the nearest integer.

Extended Data Table 1 | Prescribed microplastic surface concentrations in GCM simulations

Experiment name	Fragments (MP m^{-3})	Fibres (MP m^{-3})	Altitude range (km)
Control	0	0	-
Fragments	100	0	0 – 10
Fibres	0	100	0 – 10
Combined	50	50	0 – 10
Boundary layer	50	50	0 – 2

Extended Data Table 2 | Optical properties of microplastic fragments and fibres supplied to the GCM in the shortwave and longwave bands

Shortwave			Fragments			Fibres		
Band	Lower wavelength limit (m)	Upper wavelength limit (m)	Absorption coefficient (m^{-1})	Scattering coefficient (m^{-1})	Asymmetry factor	Absorption coefficient (m^{-1})	Scattering coefficient (m^{-1})	Asymmetry factor
1	2.00×10^{-7}	3.20×10^{-7}	1.34×10^{-11}	8.55×10^{-9}	7.95×10^{-1}	1.47×10^{-11}	1.91×10^{-8}	8.56×10^{-1}
2	3.20×10^{-7}	5.05×10^{-7}	1.01×10^{-11}	8.58×10^{-9}	8.03×10^{-1}	7.72×10^{-12}	1.91×10^{-8}	8.63×10^{-1}
3	5.05×10^{-7}	6.90×10^{-7}	1.19×10^{-11}	8.60×10^{-9}	8.07×10^{-1}	8.94×10^{-12}	1.91×10^{-8}	8.66×10^{-1}
4	6.90×10^{-7}	1.19×10^{-6}	2.95×10^{-11}	8.63×10^{-9}	8.07×10^{-1}	2.19×10^{-11}	1.91×10^{-8}	8.68×10^{-1}
5	1.19×10^{-6}	2.38×10^{-6}	1.75×10^{-10}	8.56×10^{-9}	8.09×10^{-1}	1.32×10^{-10}	1.90×10^{-8}	8.70×10^{-1}
6	2.38×10^{-6}	1.00×10^{-5}	1.30×10^{-9}	7.61×10^{-9}	8.34×10^{-1}	1.27×10^{-9}	1.79×10^{-8}	8.78×10^{-1}
Longwave			Fragments			Fibres		
Band	Lower wavelength limit (m)	Upper wavelength limit (m)	Absorption coefficient (m^{-1})	Scattering coefficient (m^{-1})	Asymmetry factor	Absorption coefficient (m^{-1})	Scattering coefficient (m^{-1})	Asymmetry factor
1	2.50×10^{-5}	1.00×10^{-2}	2.95×10^{-9}	7.75×10^{-9}	7.71×10^{-1}	2.51×10^{-9}	1.66×10^{-8}	8.89×10^{-1}
2	1.82×10^{-5}	2.50×10^{-5}	3.73×10^{-9}	6.22×10^{-9}	8.52×10^{-1}	4.11×10^{-9}	1.50×10^{-8}	9.05×10^{-1}
3	1.25×10^{-5}	1.82×10^{-5}	3.85×10^{-9}	5.77×10^{-9}	8.84×10^{-1}	4.88×10^{-9}	1.43×10^{-8}	9.14×10^{-1}
4	1.33×10^{-5}	1.69×10^{-5}	3.86×10^{-9}	5.77×10^{-9}	8.84×10^{-1}	4.88×10^{-9}	1.43×10^{-8}	9.14×10^{-1}
5	8.33×10^{-6}	1.25×10^{-5}	3.66×10^{-9}	5.69×10^{-9}	8.95×10^{-1}	4.84×10^{-9}	1.43×10^{-8}	9.14×10^{-1}
6	8.93×10^{-6}	1.01×10^{-5}	3.64×10^{-9}	5.68×10^{-9}	8.96×10^{-1}	4.82×10^{-9}	1.43×10^{-8}	9.13×10^{-1}
7	7.52×10^{-6}	8.33×10^{-6}	3.43×10^{-9}	5.80×10^{-9}	8.93×10^{-1}	4.40×10^{-9}	1.47×10^{-8}	9.08×10^{-1}
8	6.67×10^{-6}	7.52×10^{-6}	3.25×10^{-9}	5.92×10^{-9}	8.89×10^{-1}	4.04×10^{-9}	1.51×10^{-8}	9.04×10^{-1}
9	3.34×10^{-6}	6.67×10^{-6}	1.96×10^{-9}	7.01×10^{-9}	8.52×10^{-1}	1.97×10^{-9}	1.72×10^{-8}	8.84×10^{-1}